Chemical Engineering Journal 468 (2023) 143835

Contents lists available at ScienceDirect

Chemical Engineering Journal

journal homepage: www.elsevier.com/locate/cej

Photo-rechargeable battery with an energetically aligned beetroot Dye/Cl-Graphene quantum dots/MoO_3 nanorods composite

Babneet Kaur, Debanjan Maity, Ponnada Yallam Naidu, Melepurath Deepa *

Department of Chemistry, Indian Institute of Technology Hyderabad, Kandi 502284, Sangareddy, Telangana, India

ARTICLE INFO

Keywords:
Zinc
Photo-battery
Graphene
Molybdenum oxide
Storage

ABSTRACT

A stand-alone, low-cost non-aqueous photo-rechargeable zinc ion battery configuration is presented. The photo-battery integrates the functions of energy conversion and storage in a single device thus minimizing space and material requirements as well as cost. The cell is based on a photocathode with TiO_2 and MoO_3-nanorods (NRs) as the storage layers, with additional roles of electron transport layer and photosensitizer for TiO_2 and MoO_3 respectively. Photoactive beetroot (BT) dye and Cl-doped graphene quantum dots (GQDs) were also incorporated therein to yield the TiO_2/BT/Cl-GQDs/MoO_3-NRs composite photocathode for broad spectral utilization. Under irradiance, the BT dye, Cl-GQDs and MoO_3 undergo electron-hole separation, channel the electrons to the external circuit via TiO_2 through aligned energy levels and simultaneously charge the battery to ~1 V, without the application of any external bias or current. The photo-charging and discharge capacities of the photo-battery: TiO_2/BT/Cl-GQDs/MoO_3-NRs/Zn^{2+}/Zn-AC in the biased mode under an applied current density of 21 mA g^{-1} and under 1 sun irradiance (100 mW cm^{-2}, AM 1.5 G) are 104 mAh g^{-1} and 240 mAh g^{-1} respectively. The photo-charging capacity under 1 sun irradiance in the unbiased mode is ~75 mAh g^{-1}. A Zn-activated carbon composite (derived from lemon pieces) as the anode electro-catalyzes the reduction of Zn^{2+} during photo-charging, leading to a power conversion efficiency of 4.03 % under one sun illumination. This has a cycle life of 200 cycles and offers a constant photocurrent of 8.3 mA cm^{-2} with a hold time of more than 100 s under irradiance which can easily charge any small electronic device. It is an economically viable configuration with huge technological potential for possible commercialization.

1. Introduction

The world has for long has been relying on fossil fuels for its energy requirements. Though several off-grid sources such as wind and solar technologies have assisted in past years to generate energy sustainably yet efficient storage of that energy has posed a formidable challenge. One elegant solution is the use and deployment of photo-rechargeable batteries [1,2]. Here, a single device converts solar radiation to electric current and then stores the same in the form of Faradaic charge. There are several advantages to going from two devices (solar cell and battery) to a sole device where the two functions of conversion and storage are synergistically integrated. Space saving, reduced material usage (and hence lower carbon footprint), portability and better flexibility are some of the advantages of dual function photo-rechargeable batteries over the individual systems [3]. At the same time, there are also some key issues that have hindered the active development of such cells. Poor band gap structure, chemical instability due to harsh conditions, formation of by-products due to unwanted oxidation or reduction reactions, dendrite formation at the metal-electrode lead to low power and energy densities, poor cycling stability and low PCEs [3,4].

The following design considerations are helpful in overcoming the above and in developing an efficient architecture. (1) In a photo-battery, the photo-electrode's output voltage should be high enough to serve as the input charging current for storage to occur. It should also be constant and stable so that the photocurrent produced is constant as a function of time. (2) Further, the resistances at the various interfaces for charge transfer and transport need to be minimized to maximize both: (i) the power conversion efficiency (PCE) of the solar cell and (ii) the discharge capacity. This necessitates the photo-electrode to have energy levels suitably aligned for electron and hole transport via cascade mechanism and an anode that easily allows metal ion (such Li^+, Na^+, Zn^{2+} etc) reduction and metal oxidation (Li, Na, Zn etc) in the charge discharge cycles.

* Corresponding author.
E-mail address: mdeepa@chy.iith.ac.in (M. Deepa).

https://doi.org/10.1016/j.cej.2023.143835
Received 27 January 2023; Received in revised form 1 May 2023; Accepted 27 May 2023
Available online 29 May 2023

The main improvements in the work here are as follow. (1) Compared to the well-reported photo-batteries [4-10], here the composition of the photocathode is unique with a natural dye and chlorine-doped graphene quantum dots (Cl-GQDs) functioning as the photosensitizers coupled with MoO_3 nanorods (NRs) as the intercalation material as well as light harvester. (2) The energy level offsets between TiO_2, the electron transport layer (ETL), beetroot (BT) dye, Cl-GQDs and MoO_3-NRs are conducive for thermodynamically favorable hole and electron transfer phenomena under irradiance. This is one of the most important features of the photo-battery because it maximizes charge separation and therefore the output current which in turn drives the photo-charging process efficiently. (3) The non-aqueous electrolyte used is $ZnCl_2$ in γ-butyrolactone (γ-BL), which has not been used even in Zn-ion batteries (ZIBs) till date. It has a high ionic conductivity of 2.3 mS cm^{-1} at room temperature, is inexpensive, and can be handled in air unlike zinc triflate [$(Zn(OTf)_2$] or zinc imide [$Zn(TFSI)_2$] which are expensive, highly hygroscopic and can be handled only in a glove box or inert atmosphere. (4) The photo-battery can be easily assembled in air and does not require a glove box or inert atmosphere. (5) The conventional Zn foil anode is replaced by a Zn-activated carbon (AC) composite. Compared to Zn-foil which is a planar substrate, here Zn and AC are adsorbed over the mesh like framework of Ni-foam leading to an increase in the surface area of Zn exposed to the electrolyte and the mesh like structure of Ni-foam also enables improved percolation of electrolyte, which effectively lead to an improved redox activity in terms of Zn^{2+} ion reduction at the anode during photo-charging. Furthermore, the Zn-AC composite can also effectively prevent dendritic growth at the anode due to the presence of AC [11,12]. Unlike the Zn-foil anode, on which dendrites can form uncontrollably during repetitive electrochemical cycling of the photo battery, AC allows the uniform adsorption of Zn^{2+} ions over the Zn-AC anode due to the presence of oxygen containing functional groups leading to a homogeneous Zn-deposit. But with Zn-foil, the Zn^{2+} ions tend to deposit one over other due to a low activation energy and form dendrites.

A few photo-rechargeable batteries and photo-activated systems have been developed in the past based on metal-ion [13], metal-air [14], dye-sensitized electrodes [15], interfacial solar evaporation systems [16], photocatalytic hydrogen production [17] and redox flow systems [18]. There are some other benefits as well for Zn-ion systems [19,20] compared to Li-ion [10] and K-ion [21]. These include: a significantly enhanced Zn abundance in earth's crust relative to Li, the relatively lower cost of Zn, high recycling recovery efficiency of Zn, and that Zn undergoes a two-electron redox reaction instead of a one-electron one, leading to an improved energy density.

These beneficial attributes have been effectively tapped in some reported configurations. ZnO/MoS_2 grown over a carbon felt (CF) substrate-based photocathode was integrated with an aqueous $Zn(OTf)_2$ electrolyte and a Zn anode in a photo-battery (hν-ZIB). A photo-conversion efficiency of ~1.8 % was achieved at 455 nm. Photo-charging (12 mW cm^{-2} at 455 nm) in addition to electro-charging (under 100 mA g^{-1}) enhanced the battery capacity from 245 to 340 mAh g^{-1}, and the hν-ZIB also demonstrated a capacity retention of ~82 % over 200 cycles [5]. Yet another configuration employed VO_2/reduced graphene oxide (rGO) layers coated over CF as the photocathode, wherein the work function of rGO, assisted the photo-excited electron relay to the CF, increased charge separation and improved the photo-charging efficiency. The aqueous hν-ZIB achieved a capacity of ~282 mAh g^{-1} in dark and ~315 mAh g^{-1} under light, at 200 mA g^{-1}, signifying the use of light not only to charge the cell, but additionally to enhance its' capacity as well [4]. Another architecture used a photocathode co-sensitized with poly(3-hexyl thiophene) (P3HT) and V_2O_5 (for wider light absorption). The resulting CF/rGO/P3HT/V_2O_5/Zn^{2+}/Zn based hν-ZIB, showed capacities of 190 and 370 mAh g^{-1} in dark and light and a photo-conversion efficiency of ~1.2 % [6]. Another configuration used a ZnO/VO_2 photocathode and capacities of ~367 mAh g^{-1} in dark and 432 mAh g^{-1} in light at 200 mA g^{-1} were reported [7]. The fabrication of these photo-batteries is slightly complex for it entails careful drilling of a hole at the photocathode side on the cell casing to allow light penetration. These batteries also employed aqueous $Zn(OTf)_2$ solutions as the electrolyte and Zn-foil as the anode. However, aqueous electrolytes promote the formation of dendrites at the Zn-anode, which can compromise the cycle life and safety of the photo-battery.

Taking this approach forward, this study reports a hν-ZIB based on a novel photocathode architecture of TiO_2/BT/Cl-GQDs/MoO_3-NRs. Carbon cloth or felt has been used as the current collector to fabricate photo-batteries in the past [4-7] primarily because of its very low sheet resistance ($\leq$10 Ω cm^{-2}), its highly porous structure that allows high adsorption of active materials and flexibility. However, since it has a mesh like texture, it cannot allow complete penetration of solar radiation, when illuminated. Light can only pass through the pores, which results in a significantly lowered light transmission through the carbon cloth and hence leads to a poor PCE, due to insufficient absorbed light. The lowered PCE in turn adversely affects the photo-charging capability of the photo-battery. In comparison, when FTO coated glass is used as the current collector in a photo-battery, it allows excellent penetration of solar radiation or input light, and thus nearly all of the photo-active material which is tethered to FTO is able to absorb light and convert the same into electric current, thereby improving both the PCE and the photo-charging ability of the photo-battery. Furthermore, compared to FTO, carbon felt or cloth has greater chances for deteriorating, when it is brought in contact with acidic or alkaline or organic electrolytes though undesirable chemical reactions with the carbon-framework, which can lead to a rapid performance decline. Occasionally, the fiber like shapes (which carbon cloth is made of) can also unravel and leach into the electrolyte. FTO, on the other hand, is a rigid substrate, it is highly stable in such electrolyte media and due to an optimal surface roughness, it is able to firmly adsorb the active material coating, thus rendering it be an ideal conducting support for photo-battery applications.

In the present hν-ZIB, each component in the photocathode has a specific function. TiO_2 serves as the ETL and it also acts as an intercalation material for Zn^{2+} ions during the discharge process. Besides this, TiO_2 used here is a mesoporous nanomaterial with a good effective surface area, that allows a high adsorption of the photosensitizers. BT dye shows a strong absorption band over 400–600 nm. It is a fully non-toxic, cheap natural dye, thus making it ideal as a light harvesting material for the photo-battery. Here Cl-GQDs were chosen because they have a strong absorption in the blue-green region (400–500 nm) of the visible spectrum, with an optical band gap of ~1.7 eV and they are also strongly fluorescent, indicative of their ability to undergo electron-hole separation under illumination, thereby rendering them to be suitable as a co-sensitizer in the photocathode. Furthermore, they are cost-effective, non-toxic, chemically compatible with the other components of the photocathode and they are also stable in the non-aqueous electrolyte ($ZnCl_2$/γ-BL). MoO_3 NRs is the principal ion-storage material with a layered crystal structure. It allows the accommodation of Zn^{2+} ions, in-between the layers during discharge and also functions as a light harvesting material. It is the synergy between all the four components of the photocathode with suitably positioned energy levels that results in the optimal photoelectrochemical performance achieved by the photo-battery.

2. Experimental

2.1. Chemicals

Nickel foam having a thickness of 1 mm was purchased from Gelon. Fluorine doped tin oxide (FTO) having a sheet resistance in the range of ~22–25 Ω/cm^2 was purchased from Pilkington. Ammonium molybdate tetrahydrate ($(NH_4)_6Mo_7O_{24}{\cdot}4H_2O$)), nitric acid ($HNO_3$), glucose, hydrochloric acid (HCl), ethylene diamine, ethanol, zinc chloride ($ZnCl_2$), γ-butyrolactone (γ-BL), potassium hydroxide, PVdF (polyvinylidene difluoride), carbon black (CB), acetate buffer (sodium acetate/acetic

acid) and Zinc (Zn) powder were purchased from Merck. N-methyl-pyrrolidone (NMP) was purchased from Tokyo Chemical Industries. TiO_2 powder (P25, 21 nm primary particle size, 35–65 m^2 g^{-1} surface area) was obtained from Evonik. GF/D-glass micro-fiber separators were purchased from Whatman. Ultrapure water was obtained from a Millipore Direct Q3 UV-system.

2.2. Synthesis of MoO_3 nanorods (NRs)

For the preparation of nanorods of MoO_3, 0.2 M ammonium molybdate was added to 10 mL of ultrapure water and the solution was stirred for 20 min. and a clear colorless solution was obtained. Upon adding concentrated HNO_3 (15.6 M, 5 mL) to the above solution, it turned turbid and white colored products were found floating in the formulation, and it was immediately transferred to a Teflon-lined hydrothermal autoclave of 50 mL capacity. It was placed in an oven for 12 h at 180 °C. A greyish-white colored precipitate was obtained which was filtered, washed with ethanol and ultrapure water. The wet solid was dried in an oven at 70 °C for 24 h and is referred to as MoO_3-NRs [22]. Scheme 1a shows the preparation of the nanorods.

2.3. Synthesis of Cl-GQDs

To 15 mL of ultrapure water, 1 g of glucose, 200 µL of HCl and 400 µL of ethylene diamine were added and dissolved to result in a clear solution. The above solution was transferred to a Teflon-lined hydrothermal autoclave of 50 mL capacity. The autoclave was placed in an oven for 6 h at 200 °C. A brown colored dispersion of Cl-GQDs was obtained which was stored and used directly [23]. This synthesis is displayed in Scheme 1a.

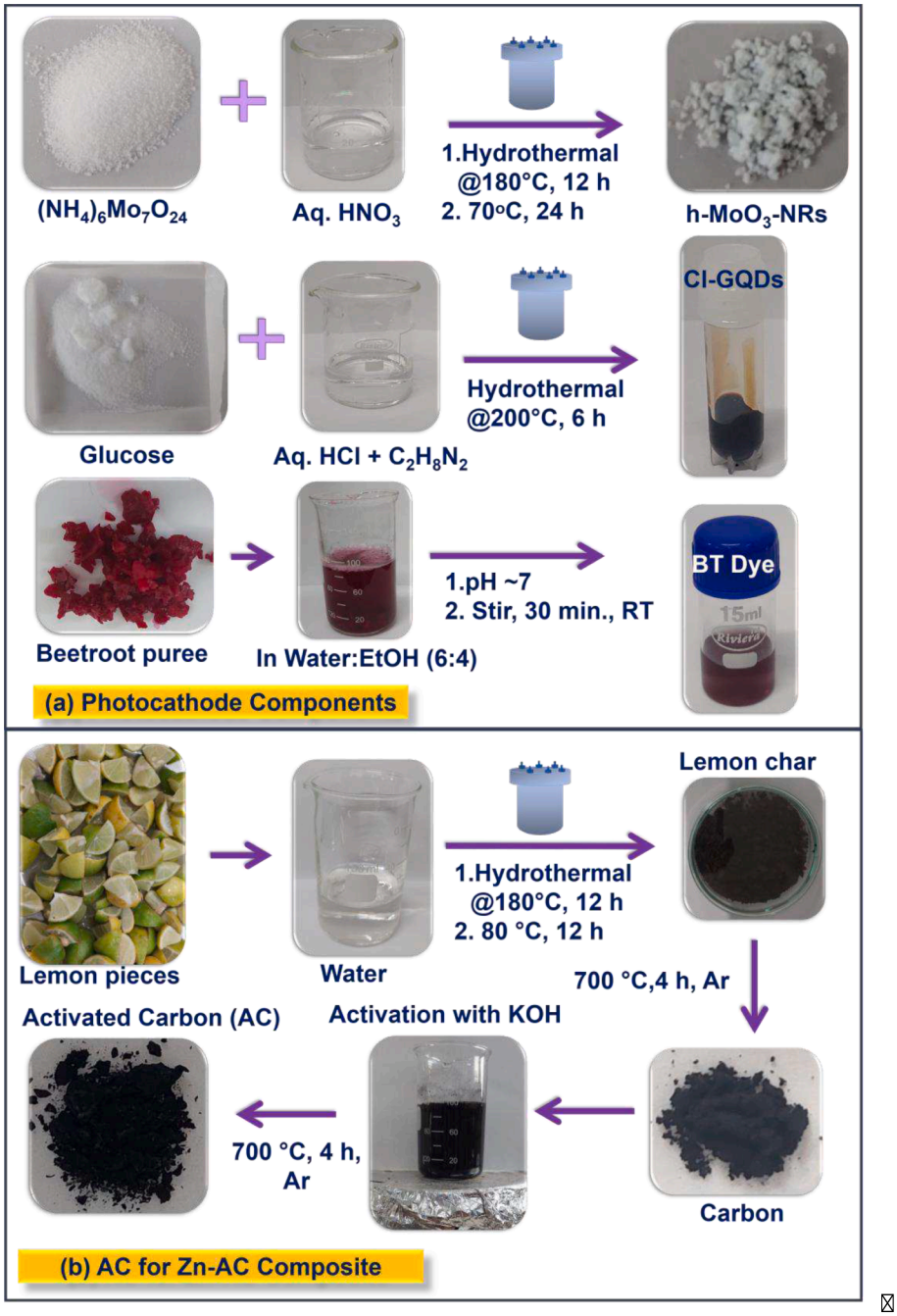

Scheme 1. Stepwise synthesis of (a) photocathode and (b) anode components of the photo-battery.

2.4. Preparation of beetroot (BT) dye suspension

Fresh beetroots were procured locally, peeled and washed with water and cut into small pieces. The beetroot pieces are grinded to make a homogeneous smooth puree. The puree (2 g) was weighed and transferred into a beaker. A solvent mixture (water: ethanol (6:4) v/v) (100 mL) was transferred into the above beaker. The pH of the solution was adjusted to 7 using an acetate buffer solution. The mixture was stirred for 30 min. at room temperature. It was filtered and the filtrate was stored in a cool place away from sunlight to be used further as a dye. Scheme 1a shows the dye-suspension.

2.5. Synthesis of lemon pieces derived activated carbon

Cut-lemon chunks (5 g) and ultrapure water (50 mL) were placed in a Teflon-lined stainless-steel autoclave of 100 mL capacity. The autoclave was placed in an oven for 12 h at 180 °C. A blackish-brown colored charred product was obtained which was filtered and dried in an oven at 80 °C for 12 h. The dried compound was taken in a ceramic crucible and kept in a tubular furnace under an Argon atmosphere at 700 °C for 4 h. A black colored carbon was obtained. For activating the carbon, KOH and carbon were taken in a beaker in a weight ratio of 2:1, 150 mL of ultrapure water was added to it and heated at 80 °C with continuous stirring for 24 h. The solution was filtered, and the product was collected and dried in oven at 80 °C for 24 h. Then it was further annealed at 700 °C under an Argon atmosphere for 4 h. The resulting product was named as activated carbon (AC), stored in air, and used. Scheme 1a illustrates the synthesis of AC.

2.6. Fabrication of photo-rechargeable Zn-ion battery

Zinc powder, AC, carbon black and PVdF were taken in a weight ratio of 7:1:1:1, and grinded together in a ball-mill and a homogeneous smooth slurry was prepared using a few drops of NMP. The prepared slurry was coated over a Ni-foam (pre-cleaned with acetone) by applying a coat and removing the excess with an OHP film followed by heating in a vacuum oven at 60 °C for 24 h to yield the Zn-AC anode. MoO_3 NRs and TiO_2 were taken in a weight ratio of 3:1 (69 mg: 23 mg), and grinded for 30 min. using a pestle-mortar assembly. To the above grinded mixture, 100 μL of each Cl-GQDs and beetroot (BT) dye suspensions were added and grinded again for 15 min. PVdF (5 mg) was added to the above mixture, grinded and a smooth uniform slurry was made using NMP. The slurry was coated on FTO glass and dried in a vacuum oven at 60 °C for 24 h to obtain the TiO_2/BT/Cl-GQDs/MoO_3-NRs photocathode. The photocathode mass loading on the FTO glass was maintained at ~ 2.5 mg cm^{-2} and the active electrode area was ~ 1.2 cm^2. A GF/D separator was wetted with a few drops of a liquid electrolyte (0.5 M $ZnCl_2$ in γ-BL) and then sandwiched between the Zn-AC composite coated over Ni-foam (anode) and the TiO_2/BT/Cl-GQDs/MoO_3-NRs electrode (photocathode) and the edges of the device were sealed using a room temperature curable cyanoacrylate sealant. Scheme 2 shows the photograph of the photo-battery and its' fabrication.

The optimal concentrations of the photoactive materials in the photocathode were determined though control experiments based on the individual materials. The concentrations of Cl-GQDs and BT dye were fixed at 100 μL each, on the basis of the PCEs achieved for cells of TiO_2/Cl-GQDs(x μL)//Zn-AC and TiO_2/BT(x μL)//Zn-AC with varying values of x (50, 100 and 200). The J-V characteristics and the photovoltaic parameters are shown in Figure S1 and Table S1. For BT dye and Cl-GQDs based cells, the highest PCEs of 1.1 % and 1.75 % were achieved at 100 μL concentrations. The PCEs decreased at higher/lower concentrations of 50 and 200 μL, for both BT dye and Cl-GQDs due to the following reasons. At lower concentration of 50 μL, the BT or Cl-GQD content is insufficient for maximum light harvesting and conversion and at a higher concentration of 200 μL, the photoactive molecules tend to aggregate and there is significant electron-hole recombination thus leading to a PCE decline.

Similarly, the concentration of MoO_3-NRs was fixed by varying the MoO_3:TiO_2 weight ratios in the TiO_2/BT/Cl-GQDs/MoO_3-NRs photocathode and by studying the charge–discharge characteristics of the full

Scheme 2. Fabrication of the photo-battery.

cells with the $ZnCl_2$/γ-BL electrolyte and Zn-AC anode, under an applied current density of 21 mA g^{-1} and 1 sun irradiance in the biased mode. Three cells with MoO_3:TiO_2 weight ratios of 2:1, 3:1 and 4:1 were fabricated; the Cl-GQDs and BT dye contents were the same in all the three cells (100 μL each). Their performances are shown in Figure S2. The specific capacities were found to be 122, 240, and 166 mAh g^{-1} respectively for the 2:1, 3:1 and 4:1 MoO_3:TiO_2 based cells. Since the highest capacity was achieved with the 3:1 wt ratio of MoO_3:TiO_2, this concentration was used in the TiO_2/BT/MoO_3-NRs/Zn^{2+}/Zn-AC photobattery.

The charge/discharge capacities of the cells were calculated using the formula given below, when the cell was operated in the biased mode.

$$Specific\ Capacity\ (mAh{\cdot}g^{-1}) = Applied\ current\ density\ (mA{\cdot}g^{-1}) \times time\ taken\ for\ charge\ or\ discharge\ (s)/3600 \quad (1)$$

Capacity was calculated using the following equation when photocharging was done in the unbiased mode under 1 sun.

$$Specific\ Capacity\ (mAh{\cdot}g^{-1}) = Photocurrent\ density\ (mA{\cdot}g^{-1}) \times time\ taken\ for\ charge\ or\ discharge\ (s)/3600 \quad (2)$$

In the above equation, the photocurrent density is the current produced by the cell under 1 sun irradiance (100 mW cm^{-2}). It is this current which drives the photo-charging process in the unbiased mode. In the above equations, the division by 3600 is done to convert seconds to hours.

2.7. Instrumental methods

X-ray diffraction (XRD) patterns for different materials were obtained on a PANalytical, X'PertPRO instrument with a Cu Kα (λ = 1.54 Å) radiation as the X-ray source. X-ray photoelectron spectra (XPS) were obtained on an Axis Supra K-ALPHA surface analysis spectrometer equipped with a monochromatic, micro-focused Al-Kα radiation (1486.6 eV) operating at a vacuum level of ~5 × 10^{-11} Torr. The survey and core level spectral resolutions were 0.1 and 1 eV respectively. Core level spectra were analyzed using a Jandel PeakFit version 4.01 software and peaks were fitted using Gaussian cum Lorentzian amplitude functions. Absorbance spectra were recorded on a LabIndia UV 3092 double beam UV–Visible spectrophotometer. Fluorescence spectra were recorded on a Horiba FluoroMax-4 spectrofluorometer. Cyclic voltammetry (CV), electrochemical impedance spectroscopy (EIS), galvanostatic charge- discharge (GCD), studies were performed on a Metrohm Autolab PGSTAT 302 N electrochemical workstation equipped with a NOVA 1.9 software for the associated data analysis. EIS studies were performed under open circuit potentials, using an ac amplitude of 20 mV and over a frequency range of 1 MHz to 0.01 Hz.

3. Results and discussion

3.1. XRD and electron microscopy of photocathode components

XRD pattern of TiO_2, Cl-GQDs and MoO_3-NRs are displayed in Fig. 1 (a-c). TiO_2 shows multiple intense diffraction peaks, with the principal ones at 2θ = 25.2°, 37.8°, 48.0°, 55.0° and 62.6° corresponding to the (101), (004), (200), (211) and (204) planes respectively of the body centered tetragonal system with unit cell parameters of a = 3.7 Å and c = 9.5 Å, in accordance with JCPDS: 21–1272. Cl-GQDs show a single broad peak at 2θ = 23.3°, which is assigned to the (002) plane of hexagonal graphite (JCPDS NO. 75-1621). The inter-planar spacing (d) is 3.8 Å which is higher than the usual d = 3.4 Å and this is due to the doping by hetero atoms such as chlorine (Cl), nitrogen (N) and oxygen (O) in the GQDs. The larger ionic radius of the hetero atoms compared to carbon, causes the widening of the inter-layer distances in the dots. The

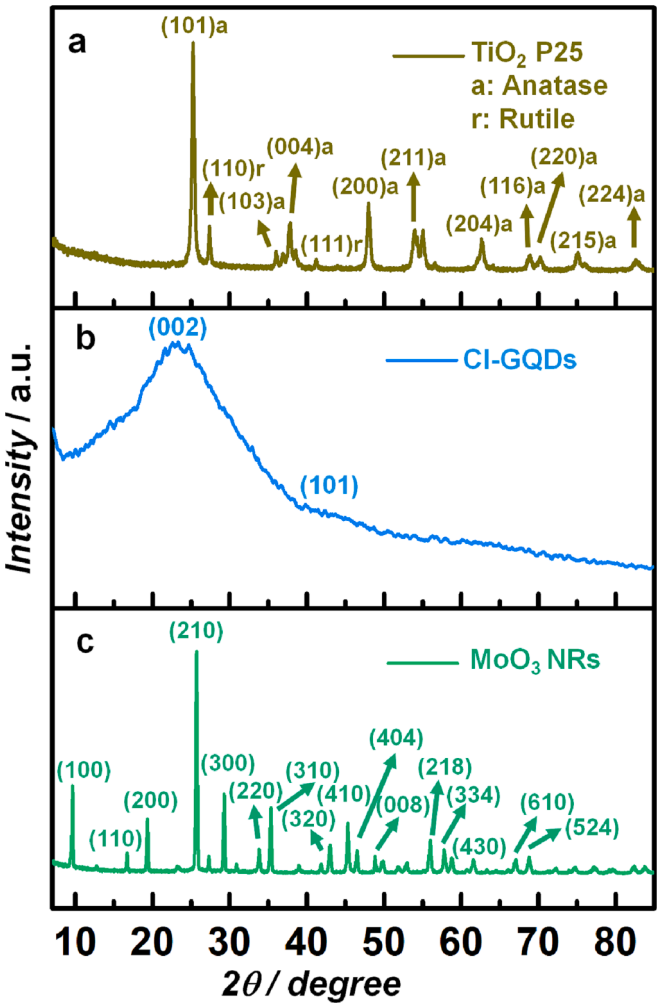

Fig. 1. XRD patterns for (a) TiO_2, (b) Cl-GQDs and (c) MoO_3-NRs.

diffractogram of MoO_3-NRs is characterized by peaks at 2θ = 9.6°, 19.4°, 25.8°, 29.3°, 35.4° and 45.4° which are attributed to the (100), (200), (210), (300), (310) and (410) planes of the hexagonal phase of MoO_3 (JCPDS No.21–0569) with the following unit cell parameters: a = 10.53 Å and c = 14.87 Å. The most intense peak is observed along the (210) plane, indicating a preferred orientation.

FE-SEM images of MoO_3 nanorods (NRs) are displayed in Fig. 2a-c. The NRs are formed in the form of bundles and have well defined smooth hexagonal facets. The latter can be judged from the high magnification image in Fig. 2c. The NRs are misaligned with respect to each other, and they are oriented in all possible directions. The images in Fig. 2b and c also clearly reveal that the rods have polygonal cross-sections, and such MoO_3 NRs have been reported earlier [24]. The widths of the NRs lie in the range of 2 to 12 μm and their lengths are found to vary from 10 to 60 μm. They are predominantly straight and are also characterized by polygonal ends or tops. The elemental mapping of MoO_3 NRs was performed to assess the phase purity of the oxide. The cumulative map shows the presence of both Mo and O along the length of the bundles of NRs (Fig. 2d). Fig. 2e and f show a highly uniform and dense distribution of the two elements (O and Mo) independently across the cross-sections of the NRs, indicative of a very homogeneous composition which is maintained for the NRs across multiple length scales. The EDX plot for MoO_3 NRs is shown in Fig. 2g, and the atomic concentrations of Mo and O are deduced to be 28 % and 71 % respectively, amounting to a stoichiometry of 1:2.53 which is close to the expected stoichiometry of 1:3. However, the ratio indicates the presence of oxygen vacancies in the lattice. The vacant sites facilitate charge transfer and transport, a feature

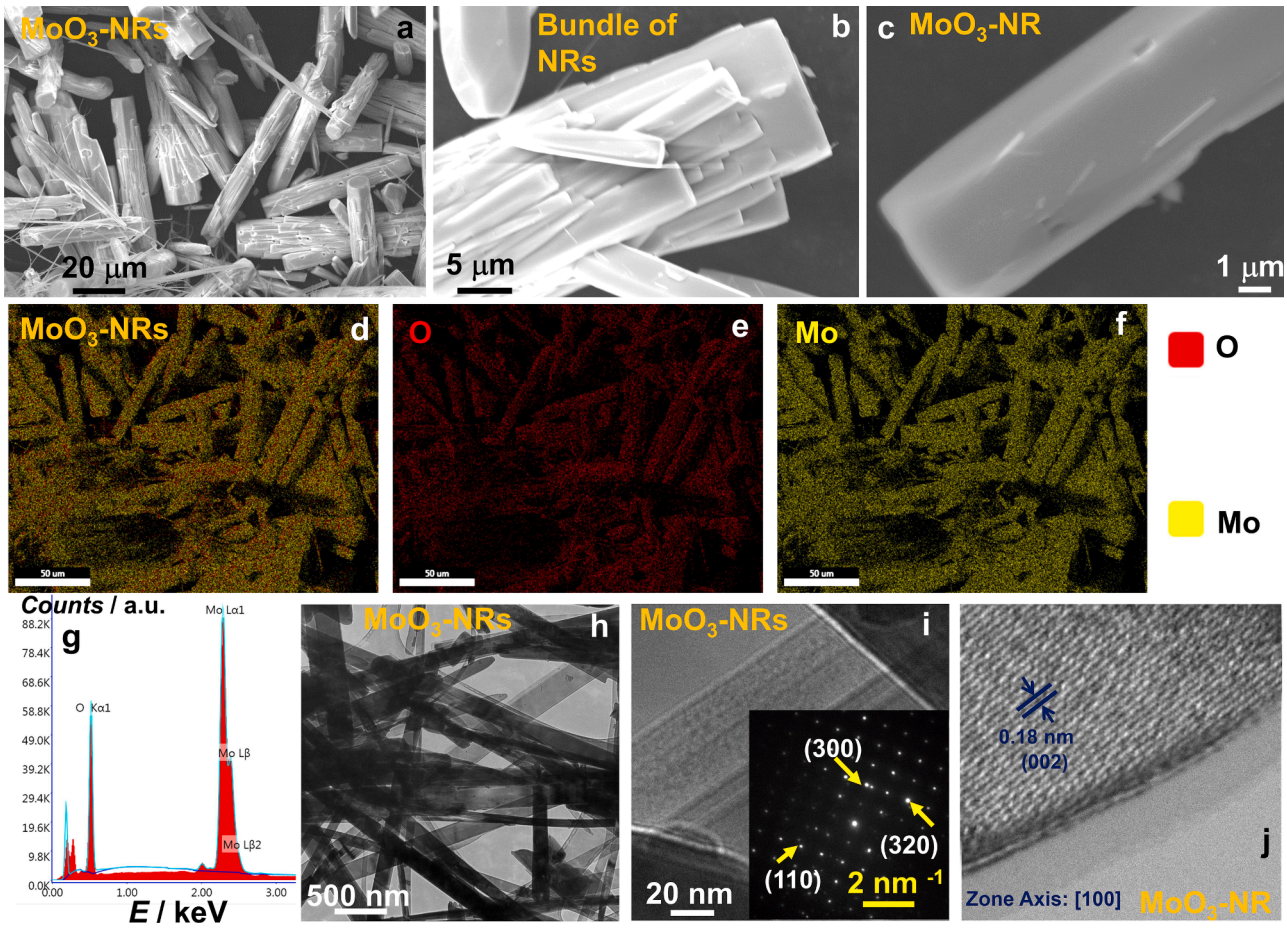

Fig. 2. FE-SEM images of (a-c) MoO_3-NRs and (d-f) corresponding elemental maps showcasing the compositional purity of the oxide. (g) EDX plot of MoO_3-NRs. (h,i) TEM images of MoO_3-NRs; inset of (i) is the SAED pattern. (j) Lattice scale image of a MoO_3-NR.

which is useful for both energy storage and conversion. Bright field TEM images of MoO_3 NRs show the rods to be arranged in a haphazard manner (Fig. 2h and i) and also to be overlapping with each other, thus concurring with the SEM observations. The high-resolution image in Fig. 2j shows the nanorods to be highly crystalline and the spacing between two adjacent fringes is 0.18 nm, which corresponds to the (0 0 2) plane of h-MoO_3. The length varies from 300 to 800 nm and the diameter from 100 to 125 nm. The zone axis is [1 0 0]. The selected area electron diffraction (SAED) pattern (inset of Fig. 2i) shows parallel rows of bright spots, and they are indexed to the (3 0 0), (3 2 0) and (1 1 0) planes of h-MoO_3.

The growth mechanism of MoO_3 NRs is as follows. In the first step, ammonium molybdate reacts with nitric acid to produce the poly(oxomolybdate) $(Mo_7O_{24})^{6-}$ species, which upon heating under hydrothermal conditions, decompose to yield the MoO_3 nucleating particles.

$$(NH_4)_6Mo_7O_{24}{\cdot}4H_2O + 6HNO_3 \rightarrow H_6Mo_7O_{24}\downarrow + 6NH4NO3\ (aq.) + 4H_2O \quad (3)$$

$$H6Mo7O24 \xrightarrow{\Delta} 7MoO3\downarrow + 3H2O \quad (4)$$

The initially formed particles are small and are therefore characterized by a high surface energy. Therefore, they aggregate via Ostwald ripening and form the thermodynamically stable larger structures which are the 1D-hexagonal nanorods. This is because MoO_3 is composed of $[MoO_6]$ octahedra in vertex-sharing and edge sharing arrangements. The anisotropic growth along the [1 0 0] direction is steered through a seed layer and stable elongated rod like structures are formed [25].

The TEM image of Cl-GQDs is displayed in Fig. 3a. Discrete Cl-GQDs with distorted spherical shapes with diameters in the range of 3 to 9 nm are observed to be uniformly distributed across the grid. The high-resolution image of Cl-GQDs in Fig. 3b reveals the finer features of the Cl-GQDs; they are crystalline and are composed of parallelly oriented lattice fringes. The inter-fringe separation is ~0.38 nm which matches with an inter-planar spacing (d) of 3.4 Å corresponding to the (0 0 2) plane of hexagonal graphite, as per JCPDS: 75-1621. The value here for Cl-GQDs is slightly enhanced due to the presence of the larger sized dopant atoms in the graphitic structure and therefore the inter-layer distance increases. Inter-fringe separation of ~0.21 nm is also observed and this concurs well with a d = 2.1 Å aligning with the (1 0 0) plane of h-graphite [26]. This "d" value represents the distance between two adjacent carbon atoms in the graphitic plane. This implies that the Cl-GQDs here, are composed of single to few layers of graphene sheet fragments with lateral dimensions less than 10 nm. The SAED pattern for Cl- GQDs (inset of Fig. 3a) shows bright spots, and they are assigned to the (0 0 2) and (1 0 1) plane of h-graphite. The TEM images of the TiO_2/BT/Cl-GQDs/MoO_3-NRs composite that doubles up as the photocathode as well as the ion-storage layer are shown in Fig. 3c and d. Clusters of irregular shaped nanoparticles are observed to co-exist with the MoO_3 nanorods. The particles with the well-defined edges are TiO_2 and the ones with fuzzy boundaries are possibly the aggregates of the dye molecules.

High resolution images in Fig. 3e and f show the presence of Cl-GQDs as well. Lattice scale image in Fig. 3e reveals inter-fringe separations of 0.5, 0.36 and 0.2 nm which are assigned to the (2 0 0), (1 0 1) and (0 0 2) planes of TiO_2 with a tetragonal structure (anatase phase). In addition, quasi-spherical particles with inter-fringe distances of 0.38 nm and 0.22 nm are also visible. They are the Cl-GQDs and the inter-fringe spacings correspond to the (0 0 2) and (1 0 0) reflections of h-graphite. Fig. 3f

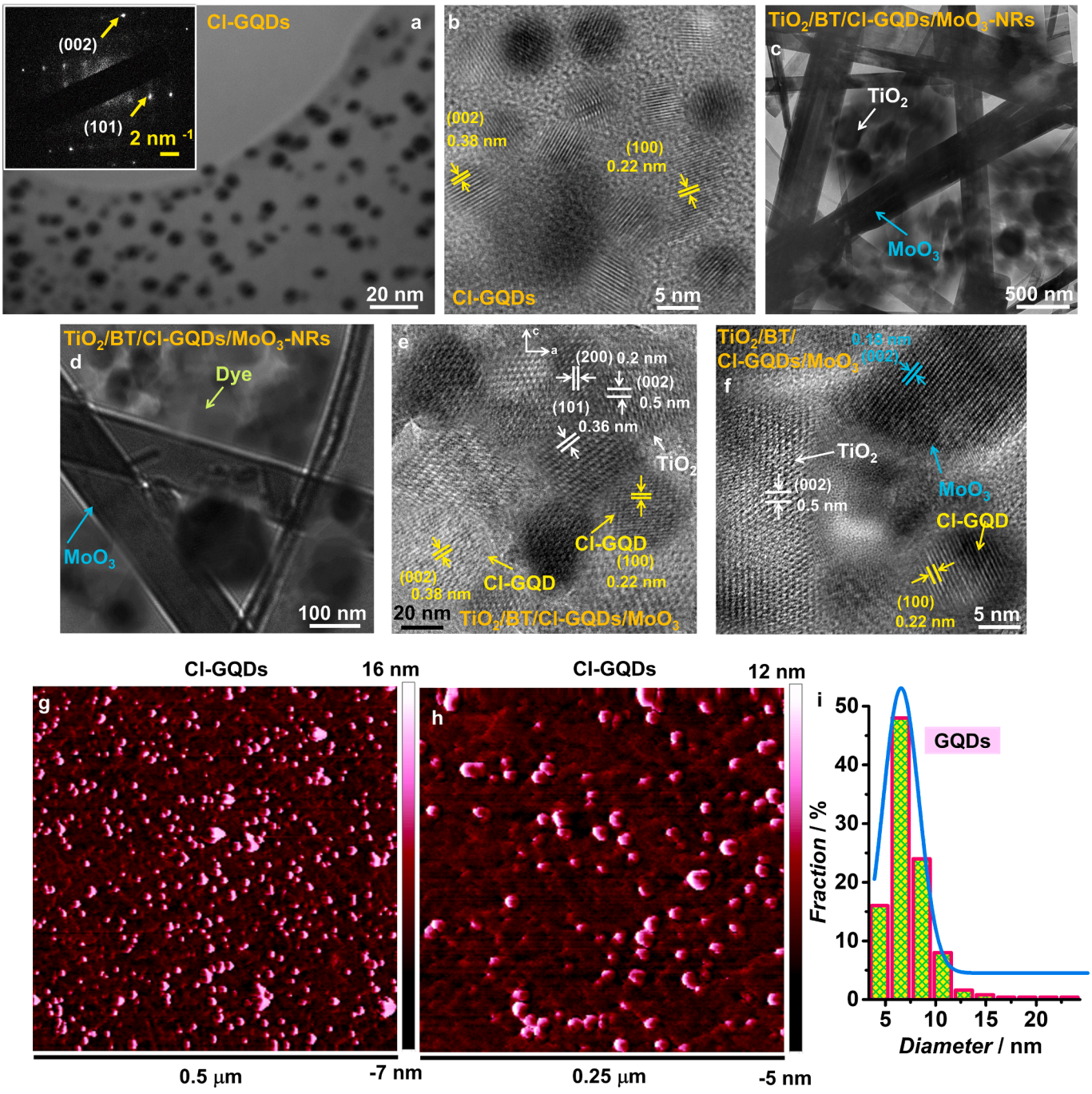

Fig. 3. (a) Low magnification TEM image and (b) lattice scale TEM image of Cl-GQDs; inset of (a) is a SAED pattern. (c,d) Low magnification TEM images of the TiO_2/BT/Cl-GQDs/MoO_3-NRs composite photocathode and (e,f) the lattice scale images of the same composite. (g,h) AFM-topography images of Cl-GQDs and (i) histogram displaying the size distribution of the Cl-GQDs.

shows the end of a MoO_3 nanorod, with a clear 0.18 nm spacing matching with the (002) plane of h-MoO_3. In this image too, lattice fringes from TiO_2 and Cl-GQDs are observed. The dye molecules are amorphous, and therefore fringes are not obtained for them. These images unambiguously confirm the nanoscale mixing of all the four components in the electrode.

The AFM topography images of Cl-GQDs are shown in Fig. 3g and h, over length scales of 0.5 and 0.25 μm. The images show a highly uniform distribution of spatially separated and discrete quantum dots. The Cl-GQDs are agglomerated only in very few regions across the sample. They are well-dispersed with size in the range of 2–27 nm, as can be perceived from the histogram for size distribution in Fig. 3i. Similar AFM images showcasing the well-separated dispersion have been reported for Cl-GQDs [26,27].

3.2. XPS analysis and I-V characteristics of composite photocathode

The survey spectrum of the TiO_2/BT/Cl-GQDs/MoO_3-NRs composite photocathode (Fig. 4a) reveals multiple strong peaks due to F1s, O1s, Ti2p, N1s, C1s and Mo3d at binding energies of 687, 530, 456, 399, 284.6 and 232 eV respectively, indicating a good mixing and presence of all the photoactive components. The F1s peak originates from the PVdF binder, used for preparing the photocathode slurry. The Cl2p signal is not observed possibly due to its low intensity. The deconvoluted Mo3d

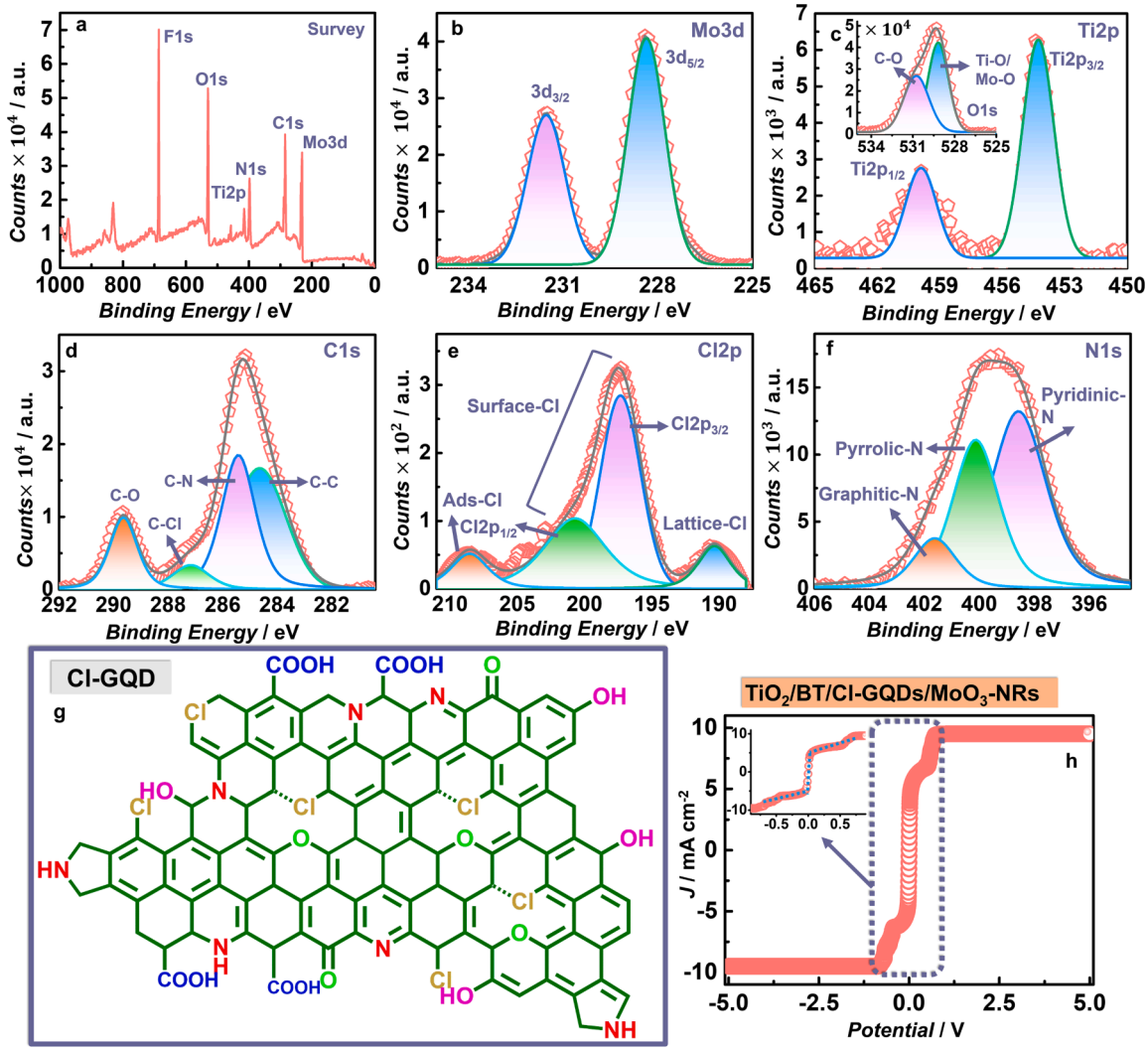

Fig. 4. XPS spectra: (a) survey spectrum and core level spectra of (b) Mo3d, (c) Ti2p (inset is O1s), (d) C1s, (e) Cl2p and (f) N1s of the TiO_2/BT/Cl-GQDs/MoO_3-NRs composite photocathode. (g) Structure of Cl-GQDs. (h) I-V characteristics of SS/TiO_2/BT/Cl-GQDs/MoO_3-NRs/SS configuration (inset is an enlarged view).

core level spectrum (Fig. 4b) shows two distinct peaks with an intensity ratio of 1.5:1, arising from the spin-orbital splitting components of $3d_{5/2}$ and $3d_{3/2}$ which are located at 228.3 and 231 eV respectively. The core level spectrum of Ti2p (Fig. 4c) upon deconvolution also gives two spin-orbital split peaks of $2p_{3/2}$ and $2p_{1/2}$ positioned at 454.4 and 459.9 eV with an intensity ratio of 1.7:1, which is close to the expected value of 2:1. The C1s core level spectrum (Fig. 4d) is highly asymmetric and after deconvolution, four peaks are obtained at 284.6, 285.4, 287.2 and 289.6 eV. These are attributed to the following covalent linkages: C-C (from the Cl-GQDs, PVdF and BT dye), C-N (from Cl-GQDs and BT dye), C-Cl (from Cl-GQDs) and C-O (from Cl-GQDs) respectively. The BT dye is composed of the nitrogen containing betaxanthin and betanin moieties and the Cl-GQDs also have graphitic, pyrrolic and pyridinic nitrogens as an integral part of the carbon framework (which are also observed in the N1s spectrum). Consequently, the C-N contribution to C1s is 35.35 %, which is second to the C-C contribution of 42.04 %. The C-Cl and C-O contributions are 6.95 % and 15.65 % respectively.

Further confirmation for the inclusion of Cl in the structure of Cl-GQD, is obtained through the deconvoluted Cl2p spectrum (Fig. 4e), which reveals four peaks. The peak at 190.3 eV with an intensity of ~9.7 % corresponds to the chloride ions attached to the edge carbons in Cl-GQDs. The j-j coupling components of $Cl2p_{3/2}$ and $Cl2p_{1/2}$ are the main contributors to the Cl2p spectrum. These peaks are observed at 197.4 and 200.7 eV, with an intensity ratio of ~1.7, and attributed to the lattice-Cl, i.e., the C-Cl-C bonds. The Cl^- adsorbed on the surface gives a peak at ~208.6 eV, with a relatively low intensity of 9 %. The deconvoluted N1s spectrum (Fig. 4f) shows three peaks with relative intensities of 51.3 % (=N-), 37.1 % (–NH-) and 11.6 % (>N-). These originate from both Cl-GQDs and BT dye. The O1s core level spectrum (inset of Fig. 4c) is deconvoluted into two peaks at 529.2 and 530.8 eV, assigned to Ti-O/Mo-O bonds from TiO_2 and the MoO_3-NRs and the C—O bonds (due to –COOH, C—O—C, C—OH) in Cl-GQDs with intensities of 55.9 % and 44.1 % respectively.

The structure of Cl-GQDs is shown in Fig. 4g wherein all the diverse bonds with the hetero-atoms can be seen clearly. XPS confirms the formation of Cl-GQDs, and affirms a good mixing of all components.

The I-V characteristics of the TiO_2/BT/Cl-GQDs/MoO_3-NRs composite photocathode recorded over a wide potential range of −5 to +5 V is shown in Fig. 4h. The plot shows a steep slope over a narrow potential range (−0.04 to +0.04 V), then shows an inclined dependence over −0.04 to −0.07 V and +0.04 to +0.75 V over negative and positive potential regimes respectively and thereafter the current saturates as a function of applied bias. This plot is characteristic of high electrical conduction across the cross-section of the composite. The dc electrical conductivity is estimated to be 4.98 mS cm^{-1}. Such a high conductivity facilitates charge transport across the thickness of the photocathode during photo-charging and discharge.

3.3. Optical properties of photocathode components

UV–visible absorption spectra of BT dye, Cl-GQDs, TiO_2, MoO_3-NRs and the TiO_2/BT/Cl-GQDs/MoO_3-NRs composite are shown in Fig. 5a. BT dye shows a broad absorption band ranging from 350 to 550 nm and tapering off in the red region with a band gap (E_g) of 1.8 eV. Multiple λ_{max} are observed over this wavelength range at ~410, 478 and 536 nm. The conjugated double bond system of the of two pigments: betaxanthin (450–500 nm) and betanin (500–550 nm), which are the constituent chromophores in the BT dye are responsible for these absorptions and consequently the vivid color [28]. Cl-GQDs show characteristic absorption peaks with λ_{max} of ~300 and ~362 nm [23], which are assigned to the $\pi - \pi^*$ and n-π^* electronic transitions of the C═C and C—N bonds and the oxygen containing bonds such as C═O, C—OH, C—O—C and C—Cl. The wide absorption band extends from the UV to visible region, then decays exponentially and the band gap is estimated to be ~1.7 eV. Similar spectral features have been reported for Cl-GQDs in earlier reports [26,29].

For all photoactive materials, the highest occupied molecular orbital (HOMO)- and lowest unoccupied molecular orbital (LUMO)- levels were calculated by combining CV (recorded in aqueous KCl) and optical absorption data (Figure S3 and Table S2). For Cl-GQDs, the LUMO and HOMO levels are located at −2.9 eV and −4.6 eV respectively. The λ_{max} for TiO_2 is observed at 316 nm and being a wide band gap semiconductor, the Eg is ~3.2 eV. MoO_3-NRs show a strong absorption band in the UV region centered at ~356 nm followed by a small shoulder peak in the visible region with λ_{max} at ~430 nm, and an E_g of 2.3 eV. Small polaron absorption (i.e., the Mo^{5+}/Mo^{6+} sites and the associated crystal lattice distortion) and quantum confinement effects in the 1D NRs gives rise to the lower energy peak. The higher energy one corresponds to the transitions at the band edge. The HOMO and LUMO levels are −4.3 eV and −2.0 eV respectively. The TiO_2/BT/Cl-GQDs/MoO_3-NRs composite shows a cumulative absorption profile such that almost all of UV and visible regions are fully absorbed by the composite. This is because of the co-sensitization effect. The photocathode assembly allows visible light utilization in the range of 400 to 700 nm. Distinctive strong and narrow peaks are observed at λ_{max} = 287, 321 and 381 nm, followed by a broad band in the visible region, with λ_{max} at 485 and 591 nm. Thereafter the absorption declines monotonically and merges with the baseline at ~700 nm. This clearly shows that this composite photocathode allows maximum utilization of UV–visible regions, and this effectively maximizes the conversion of absorbed radiation to electrical current. It is this current which drives the charging process of the photo-battery.

Cl-GQDs dispersed in water exhibit a strong excitation wavelength dependent fluorescence (Fig. 5b). Upon varying the excitation wavelength (λ_{ex}) from 320 to 440 nm, the emission maxima (λ_{em}) show a gradual red-shift from 422 to 505 nm. As discussed above, the surface trap states and the edge states in GQDs (C = C, C—N, C—O and C—Cl) exhibit the two electronic transitions ($\pi \rightarrow \pi^*$ and $n \rightarrow \pi^*$). These are followed by the radiative electron-hole recombinations from $\pi^* \rightarrow \pi$ and

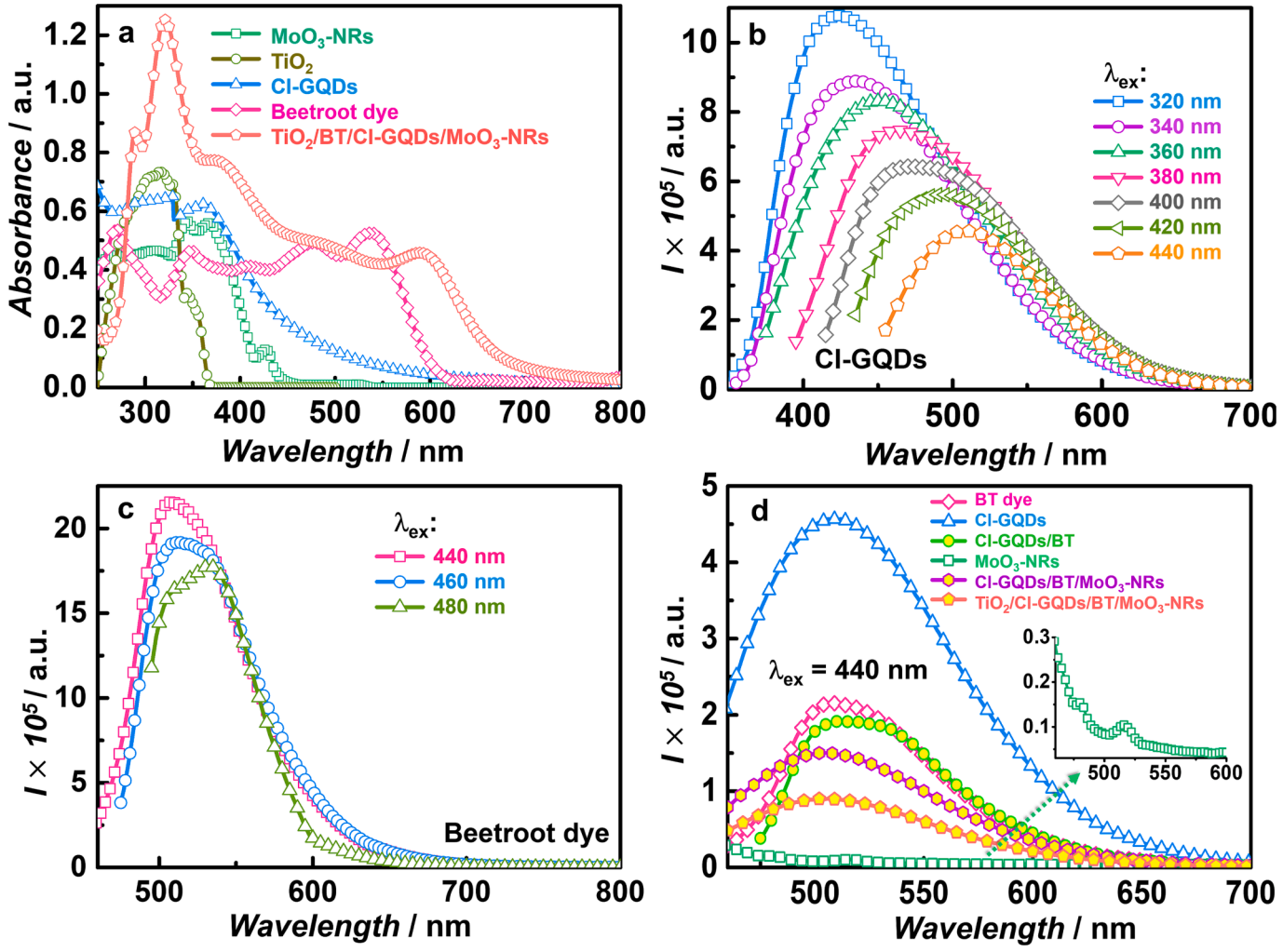

Fig. 5. (a) Absorbance spectra of MoO_3, TiO_2, Cl-GQDs, BT dye and TiO_2/BT/Cl-GQDs/MoO_3-NRs composite photocathode. (b) Fluorescence spectra of (b) Cl-GQDs, (c) BT dye at different excitation wavelengths and (d) Composites and comparison with individual components, inset shows the spectrum for MoO_3-NRs.

π*→n states leading to the observed broad emission in the visible region. The reason for decreasing intensity of the emission peak and the huge positional shift of λ_{em} by ~83 nm is attributed to the polar solvent and is called the "giant red-edge effect" [30]. When GQDs are dispersed in a polar medium, the solvation dynamics slows down to the same time scale as the fluorescence owing to the local chemical environment of the dots. Therefore, the fluorescence peak broadens and undergoes the observed red shift [30]. BT dye exhibits a broad emission band in the visible region with a λ_{max} at 508 nm (Fig. 5c). The peak position and profile do not alter much upon varying the excitation wavelength. The peak is due to the transitions between the intra-gap states.

When BT dye is added to Cl-GQDs, the PL intensity of the mixed materials is quenched by ~53 %; the decrease in intensity is attributed to the electron transfer from the conduction band (CB) of Cl-GQDs to the CB of BT dye due to favorable energy level alignment of their CBs (Fig. 5d). Inset of Fig. 5d shows the fluorescence spectrum of MoO_3-NRs (λ_{ex} = 440 nm). A distinct peak is observed at 515 nm, and a shoulder peak is observed at 478 nm. The higher energy peak is attributed to electron-hole recombination at the band edge. The lower energy one is possibly due to the transitions in-between the intra-gap defect states, due to oxygen vacancies or adsorbed –OH groups on MoO_3 surface. Similar twin peaks have been observed in earlier reports on h-MoO_3 [31,32]. The fluorescence of the composite: TiO_2/BT/Cl-GQDs/MoO_3-NRs is considerably quenched in comparison with BT dye and Cl-GQDs. This confirms the fast and efficient electron relays from the photosensitizers to TiO_2, which are discussed in detail in the next section.

3.4. Operational mechanism of the photo-battery

The photo-battery configuration is: TiO_2/BT/Cl-GQDs/MoO_3-NRs/Zn^{2+}/Zn-AC. The photo-charging of the photo-battery (under zero external bias or current) is explained here. Under one sun illumination, in BT dye, Cl-GQDs and MoO_3-NRs, the impinging photonic energy ($h\nu$) excites the electrons present in their valence bands (VBs) to their CBs, as shown in the energy band diagram in Scheme 3b. Photoexcited electrons are injected from the CB of MoO_3 NRs to that of Cl-GQDs and then to BT dye and finally to that of TiO_2. Simultaneously holes are transferred from the VB of BT dye to that of Cl-GQDs and then to that of MoO_3-NRs. These processes are thermodynamically allowed due to the favorable energy level alignments. The photo-excited electrons are then transmitted to the external circuit from TiO_2 and they reach the counter electrode of Zn-AC composite. The presence of these electrons in the CE serves as the driving force to the Zn^{2+} ions present in the electrolyte to diffuse to the CE and undergo reduction to form elemental Zn.

$$xZn^{2+} + 2xe^- \rightarrow xZn(s) \quad (5)$$

The discharge process occurs in dark, under an applied current density, as can be seen in Scheme 3a. In dark, the electron-hole pairs are not generated anymore in the TiO_2/BT/Cl-GQDs/MoO_3-NRs composite.

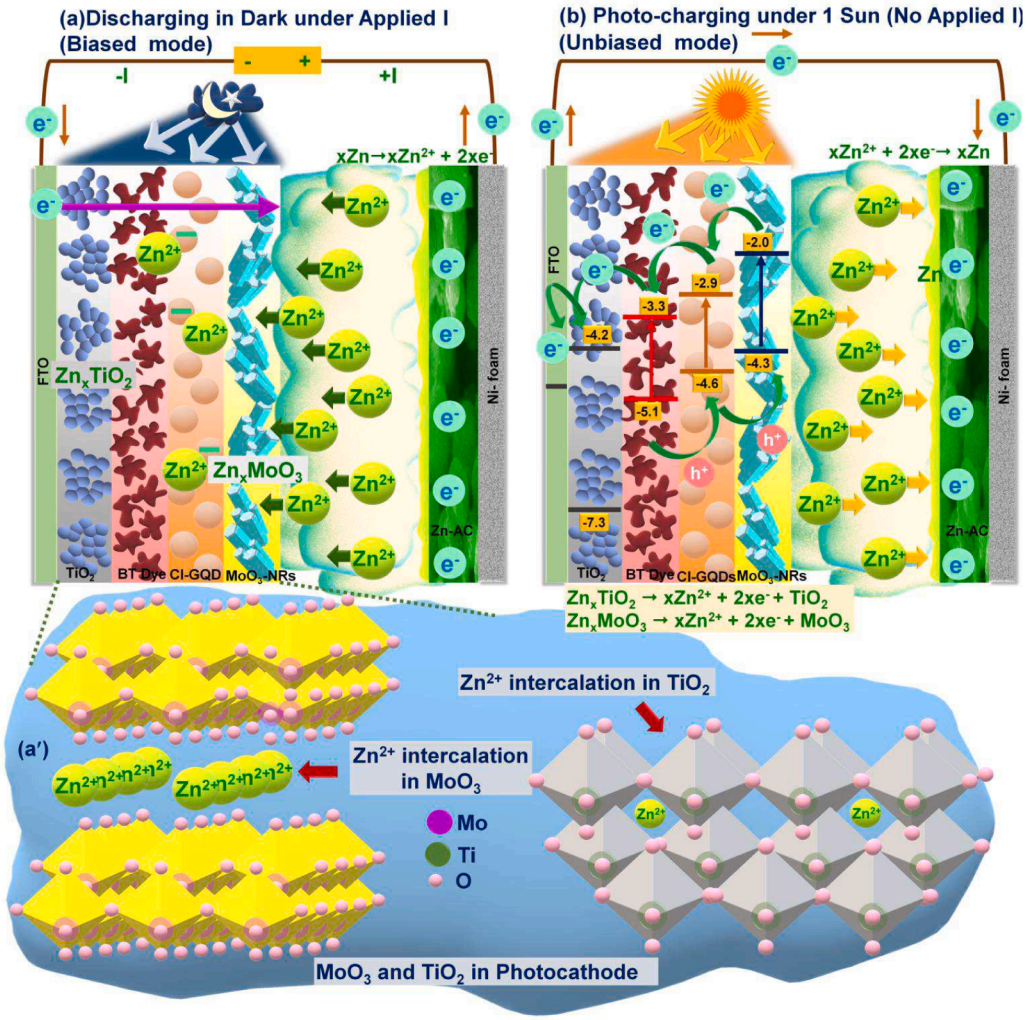

Scheme 3. Schematics illustrating the working of a TiO_2/BT/Cl-GQDs/MoO_3-NRs/Zn^{2+}/Zn-AC photo-battery: (a) discharge under applied current in dark in biased mode and (b) photo-charging under 1 sun illumination and without any applied voltage or current (unbiased mode). (a′) intercalation of Zn^{2+} in MoO_3 and TiO_2.

Furthermore, the applied electric current to this cell, now brings about oxidation of Zn to Zn^{2+} at the CE and drives the Zn^{2+} ions across the electrolyte to migrate to the composite and diffuse through its cross-section. Since all the photoactive layers are porous and allow ion-conduction, Zn^{2+} ion transport is facile, and the following Faradaic reactions (reduction) occur. Both TiO_2 and MoO_3 are intercalation type oxides, where h-MoO_3 has a layered structure composed of chains of MoO_6 octahedra with wide inter-layer spacings and TiO_2 has octahedral voids that permit the accommodation of Zn^{2+} ions. Scheme 3a′ shows how Zn^{2+} ions are hosted with ease by the MoO_3 and TiO_2 lattices.

$$Zn^{2+} + 2xe^- + MoO_3 \text{ or } TiO_2 \rightarrow Zn_xTiO_2 \text{ or } Zn_xMoO_3 \quad (6)$$

Simultaneously, it must be noted that there are some disadvantages of using a co-sensitized three stage dye system. These are enumerated here and illustrated in Scheme S1 (Supporting Information). (1) Electron-hole recombination within the individual material itself (after photo-excitation) or between any two photosensitizers (e.g., between BT dye and Cl-GQDs or Cl-GQDs and MoO_3-NRs) or even between TiO_2 and any of the photosensitizers (e.g., BT dye). (2) Besides recombination, there are also intra-gap trap or defect states present in semiconducting oxides like MoO_3 and TiO_2 (due to the presence of oxygen vacancies) and graphene-type materials like Cl-GQDs (defect states introduced by the oxygen containing functional groups attached to the carbon framework). These trap states are usually located slightly below the CB or above the VB of the semiconductor. The photo-generated electrons in the material (instead of travelling to the external circuit) can easily jump into the trap states causing a loss of electronic charge. Similarly, holes can also be scavenged by the trap states in Cl-GQDs.

Generally, a high theoretical optical voltage can be achieved experimentally if electron-hole separation is maximized in the photocathode via maximum transfer of photo-excited electrons to the external circuit. However, the above-described phenomena of (1) electron-hole recombination and (2) electron/hole injection into trap states can directly impact and reduce the theoretical optical voltage of the photo-battery, which results in a decrease in PCE and consequently, a decrease in the Zn^{2+} ion-storage capacity of the photo-battery.

3.5. Performance of the photo-battery

The TiO_2/BT/Cl-GQDs/MoO_3-NRs/Zn^{2+}/Zn-AC cell was photo-charged under AM1.5 G, 1 sun illumination (unbiased mode) and discharged in dark under different discharge current densities of 14, 18, 32,

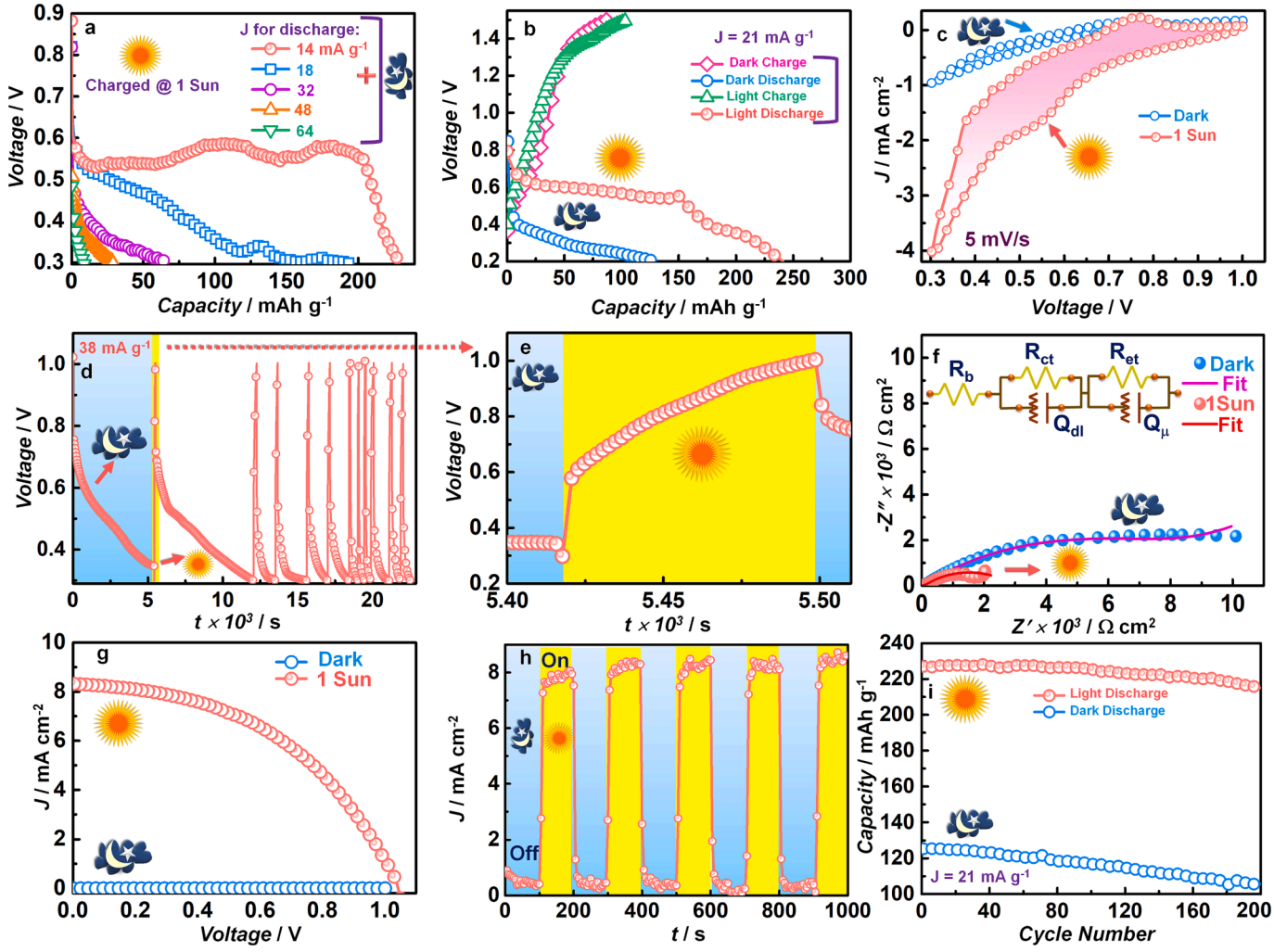

Fig. 6. All plots are for the TiO_2/BT/Cl-GQDs/MoO_3-NRs/Zn^{2+}/Zn-AC photo-battery. (a) Discharge plots (under different current densities, biased mode) in dark of the cell photo-charged to ~1 V (under 1 sun, AM 1.5G, 100 mW cm^{-2}). (b) Charge/discharge plots in dark and under 1 sun at 21 mA g^{-1} (biased mode) and (c) Comparison of CV plots (d) Photo-charging (under 1 sun, enlarged view in (e), unbiased mode) and discharging in dark under different current densities in biased mode. (f) Nyquist plots of the cell in dark and under 1 sun; inset is the equivalent circuit used for fitting the data (g) J-V characteristics under dark and 1 sun illumination. (h) Photocurrent versus time transients under light on–off cycles at a frequency of ~0.005 Hz. (i) Cycling stability of the TiO_2/BT/Cl-GQDs/MoO_3-NRs/Zn^{2+}/Zn-AC photo-battery: discharge capacity versus cycle number under light and dark at a current density of 21 mA g^{-1} (biased mode).

48 and 64 mA g^{-1} (biased mode). The discharge profiles are displayed in Fig. 6a. In the discharge cycle in biased mode, under the lowest current density of 14 mA g^{-1}, the Ohmic drop occurs till ~0.55 V and thereafter a plateau like response is obtained leading to a Zn^{2+} ion storage capacity of 227 mAh g^{-1}. Here, the capacity decreases from ~227 to ~8.2 mAh g^{-1} when the current density was increased from 14 to 64 mA g^{-1}. The capacity declines by a great extent at high current densities due to the following reason. In the photocathode, both TiO_2 and MoO_3 are intercalation type materials. Therefore, the Zn^{2+} ion intercalation process is controlled by diffusion and is kinetically a slow process. At high current densities or under fast kinetics, ion-intercalation is affected and hence the capacity is low.

The light driven charge storing and charge releasing abilities of the photo-battery were further confirmed by charging and discharging the cell in the biased mode, at a current density of 21 mA g^{-1} under 1 sun and in dark (Fig. 6b). The discharge capacities are 240 and 127 mAh g^{-1} respectively under illuminated and dark conditions in biased mode. Scheme 4 illustrates all the four scenarios, when the photo-battery is operated in biased mode. Under illumination, the discharge capacity increased by ~2 times compared to that obtained in dark. (1) In light, the photo-excited charge carriers intrinsically generated by electron-hole pair separations in semiconducting MoO_3-NRs and Cl-GQDs as well as in the visible light absorbing BT dye, increase the number of charge carriers available for circulation in the overall cell. Thus, both inherent (photo-generated) and external carriers (generated by applied I, in the biased mode) contribute to discharge and increase the formation of Zn_xTiO_2 or Zn_xMoO_3. This results in an increased discharge capacity in light compared to dark. (2) Contrastingly, in dark, only the charge carriers injected by the externally applied current contribute to the discharge capacity. Light induced charging and discharging is slower than charging and discharging under dark due to the presence of additional charge carriers in illuminated condition. (3) During charging in dark coupled with applied current in the biased mode, the electrons produced by the oxidation of Zn_xTiO_2 or Zn_xMoO_3 are channeled to the external circuit. (4) However, in light, besides this, the photo-excited electrons are also channeled into the external circuit. These electrons reach the Zn-AC electrode, and thus provide an additional driving force (akin to a light induced electric field across the two electrodes) for Zn^{2+} ions to diffuse from the photocathode and the electrolyte to the Zn-AC electrode. Thus, the charging capacity in light is also larger than that in dark under applied current.

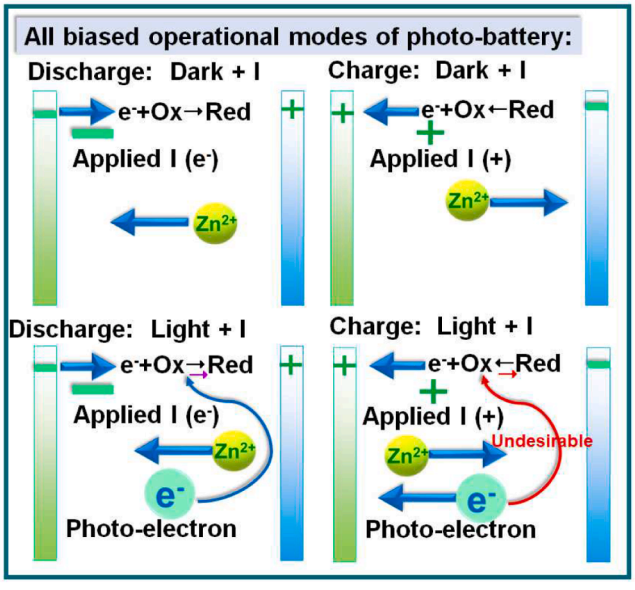

Scheme 4. Cartoons illustrating the biased processes for the plots obtained in Fig. 6(b).

To confirm the role of TiO_2, a cell with sole TiO_2 at the photocathode: FTO/TiO_2/Zn^{2+}/Zn-AC, was studied. The cell delivers a discharge capacity of ~10.3 mAh g^{-1} under the same conditions of an applied current density of 21 mA g^{-1} and under 1 sun irradiance (100 mW cm^{-2}), in the biased mode (Figure S4). Although the ion-storage capacity is low, nonetheless, it does prove the ability of TiO_2 to serve as an intercalation material.

Similarly, to evaluate the effect of Cl-GQDs on photo-battery performance, the electrochemical performance of a photo-battery without Cl-GQDs in the photocathode was examined (Figure S5). The device configuration was TiO_2/BT/MoO_3-NRs/Zn^{2+}/Zn-AC. The device shows a lower specific (discharge) capacity of 168 mAh g^{-1} compared to 240 mAh g^{-1} (with Cl-GQDs) under exactly similar conditions of applied current density of 21 mAh g^{-1} and 1 sun irradiance (biased mode). This shows the role of Cl-GQDs in improving the photo-battery's performance.

The rate capability of the photo-battery was measured by charging the cell under AM 1.5G, 1 sun illumination (in unbiased mode) and discharging it in dark at 38, 45 and 60 mA g^{-1} (in biased mode). The corresponding voltage versus time plot is shown in Fig. 6d. Again, fast charging and slow discharge are achieved especially at low current density, and this is evident in the enlarged view in Fig. 6e. The photo-charging/discharging of the photo-battery was also tested in the biased mode at different current densities of 38, 45 and 60 mA g^{-1} and irradiance (1 sun). The discharge capacity is ~160 mAh g^{-1} at 38 mA g^{-1} (Figure S6). The capacity of unbiased optical photo-charging was ~75 mAh g^{-1}. Scheme 3b illustrates the working mechanism of the cell in this mode. In this mode, capacity is moderately high, because of the Zn^{2+} ions that are released from the photocathode into the electrolyte under irradiance. The incident light drives the release of electrons and Zn^{2+} ions from the photocathode, thereby enabling photo-charging and resulting in the observed capacity under light charging in the unbiased mode.

Cyclic voltammetry (CV) studies of the photo-battery were carried out under dark and AM 1.5G, 1 sun illumination at 5 mV s^{-1} within the potential range of 0.3 to 1.0 V (Fig. 6c). The area enclosed within the CV increased by 18 % under illumination which reinforces that this is indeed a photo-battery. Under dark, the oxidation and reduction peaks of the cell are observed at ~0.7 and ~0.5 V respectively but under irradiance, the oxidation and reduction peaks are observed at ~0.75 and ~0.54 V respectively. This slight shift towards positive potentials for oxidation/reduction processes demonstrates the thermodynamic feasibility of the process.

The J-V characteristics of the cell were measured to understand the photo-response property of the composite (Fig. 6g). The cell gives an open circuit voltage (V_{OC}) = 1 V and a short circuit current density of 8.3 mA cm^{-2} under illuminated condition. This photocurrent produced by the cell is stable and consistent and this is judged from the photo-current versus time transients shown in Fig. 6h. This was measured under light on–off cycles for 50 s each, under no electrical input. Under irradiance the photocurrent produced is 8.3 mA cm^{-2}, and in dark it reduces to nearly zero. The stable photocurrent output (of ~8.3 mA cm^{-2}) achieved over a ~100 s, on a repetitive basis, is a clear indicator of how efficient this photo-battery will be for powering any small-scale electronic device.

Nyquist plots recorded for the photo-batteries under irradiance and dark conditions, over a frequency range of 1 MHz to 0.01 Hz by applying ac perturbation potential (V_{ac}) of 20 mV superimposed over the open-circuit potential (V_{dc}), are shown in Fig. 6f. The data is fitted to the [R(RQ(RQ))] Randles circuit where bulk resistances (R_b) are 30 and 27 Ω cm^2 under dark and illumination respectively. The resistance offered by the CE to charge transfer (R_{ct}) decreases from 70 to 17 Ω cm^2 ongoing from dark to light. Similarly, the electron transport resistance within the thickness of the TiO_2/BT/Cl-GQDs/MoO_3-NRs composite (R_{et}) in dark is 8.8 kΩ cm^2 and under illuminance, it is 1.8 kΩ cm^2. It is observed that all

the resistive components decrease under irradiance (compared to their values in dark). This is due to the fact, that under illumination, more number of photoexcited carriers are generated and since electrical conductivity (σ) is directly proportional to the number of mobile charge carriers per unit volume (n) through the relation: $\sigma = n \times e^{-} \times \mu$, conductivity increases and electrical resistance to charge transfer or transport decreases.

The cycling stability of the cell is presented in Fig. 6i. The cell was photo-charged and discharged under 1 sun and 21 mA g^{-1} in biased mode. The capacity decreased from 227 to 215 mAh g^{-1} over 200 cycles, implying 94.7 % capacity retention. The reasonable loss in capacity indicates that the cell is fairly robust and can endure both photo-exposure and repetitive ion-ingress and egress without undergoing any major degradation. Table S3 provides a comparison of the performance parameters of hν–ZIBs reported in literature and our work. For the photo-battery under study, despite the high loading of 2.5 mg/cm^2, and a non-fully transparent electrode for light transmission, the discharge capacity achieved under dark and light (with applied I) in the biased mode are high. Further, all the components of the cell are eco-friendly and the cell is extremely easy to assemble and use. The materials and the cell are scalable, thus making it one of the most attractive photo-battery configurations till date.

3.6. Electrocatalytic properties of the Zn-AC composite anode

FE-SEM images of Zn-AC composite are shown in Fig. 7(a,b). The low magnification image shows irregular shaped particles, inter-linked with each other. The Zn particles are spherical in nature (as can be perceived in Fig. 7b), and they are juxtaposed with the AC-particles and therefore charge transfer and transport in-between the particles are facile which contributes to the good electrochemical response of the photo-battery. The electrocatalytic behavior of the Zn-AC composite/Ni-foam electrode was evaluated from the linear sweep voltammogram recorded in a solution of 0.5 M $ZnCl_2$ in γ-BL as the electrolyte over a potential range of −0.95 to 0.6 V (inset of Fig. 7c). A broad reduction peak at 0.005 V was observed with respect to Ag/AgCl/LiCl-EtOH which is about ~0.145 V versus NHE. This peak corresponds to the reduction of Zn^{2+} to Zn. Thus, the reduction occurs at a higher positive potential compared to the standard reduction potential (-0.76 V versus NHE) of the $Zn^{2+/}$Zn couple. The reduction is facilitated due to the nanostructured nature of the electrode, which is Zn-nanoparticles embedded in an AC scaffold. The ability of the Zn-AC composite to undergo facile reduction is also further confirmed from the Nyquist plot recorded for a symmetric cell of Zn-AC/Zn^{2+}-γ-BL/Zn-AC (Fig. 7c). A skewed semi-circular response was obtained which was fitted into a R(QR) circuit. The bulk resistance R_b is ~25 Ω cm^2 and the R_{ct} is ~28 Ω cm^2. This low value of R_{ct} reaffirms that Zn^{2+} reduction occurs very easily at the Zn-AC/Zn^{2+}-γ-BL interface.

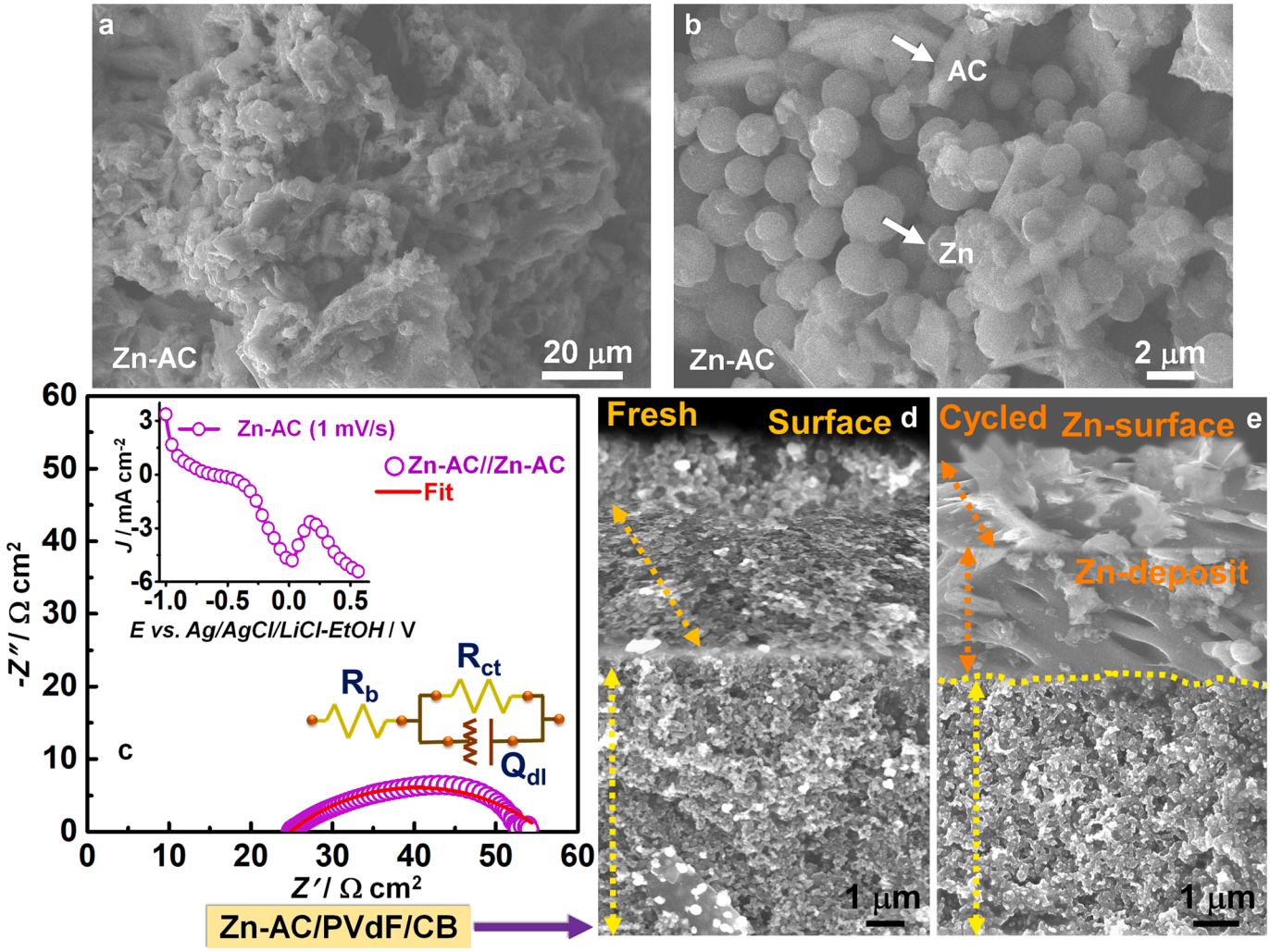

Fig. 7. (a,b) SEM image of Zn-AC. (c) LSV plot of a Zn-AC/Ni-foam electrode in a 3-electrode cell, with Pt as CE, Ag/AgCl/LiCl-EtOH as reference and 0.5 M $ZnCl_2$/γ-BL as the electrolyte. (d) Nyquist plot of a Zn-AC//Zn-AC symmetric cell; inset shows the equivalent circuit used for fitting the data. Cross-sectional FE-SEM images of (d) fresh and (e) cycled Zn-AC composite anodes.

The cross-sectional FE-SEM images of fresh and cycled Zn-AC anodes are shown in Fig. 7e,f. The fresh Zn-AC composite anode shows a continuous network of interconnected particles indicative of a good mixing of Zn particles, the carbonaceous particles, the polymer (PVdF) and CB (Fig. 7e). Post-cycling (after 200 charge–discharge cycles, at 21 mA g^{-1} and under 1 sun, in biased mode), the image of the cycled Zn-AC anode (Fig. 7f) shows the uniform deposition of elemental Zn over the Zn-AC anode. The thickness of the Zn deposit is ~3.1 μm and there is no spike like growth which is usually associated with dendrites. This is indicative of a good electrochemical cycling stability. Both the non-aqueous electrolyte and the presence of AC in the anode here contribute to preventing dendritic growth of Zn, which is typically observed in aqueous Zn-ion batteries [33-35].

4. Conclusions

In this work, a unique rapid-charging photo-battery of TiO_2/BT/Cl-GQDs/MoO_3-NRs/Zn^{2+}/Zn-AC is developed and demonstrated. This cell is a stand-alone cost-effective system assembled in air, thus rendering it to be a viable option as a power source for small scale electronic devices. In the photocathode, the band offsets are low between different materials minimizing electron recombination and maximizing electron-hole separation via directed electron and hole pathways. The TiO_2/BT dye/Cl-GQDs/MoO_3 assembly allows visible light utilization from ~400 nm to ~700 nm, enabling photo-charging to 1 V under 1 sun irradiance in the unbiased mode corresponding to a capacity of ~75 mAh g^{-1}. The discharge capacities achieved in the biased mode under 21 mA g^{-1}, are 127 mAh g^{-1} (dark) and 240 mAh g^{-1} (light, 1 sun irradiance), showcasing that the cell allows additional Zn^{2+} intercalation under light. The cell endures 200 cycles of photo-charging and discharge (under applied current, in biased mode) with 94.7 % retention of its initial capacity, suggestive of the efficacy of the architecture in facilitating charge transfer and transport for maximum solar conversion as well at Zn^{2+}-ion storage due to its nanostructured, energetically aligned components.

Declaration of Competing Interest

The authors declare that they have no known competing financial interests or personal relationships that could have appeared to influence the work reported in this paper.

Data availability

Data will be made available on request.

Acknowledgments

Financial support for this work from the Science & Engineering Research Board (SERB) of India (Grant no. CRG/2020/000482) is gratefully acknowledged by M. Deepa and B. Kaur. B.K. is thankful to PMRF scheme for PhD fellowship.

Appendix A. Supplementary data

Supplementary data to this article can be found online at https://doi.org/10.1016/j.cej.2023.143835.

References

[1] S. Ahmad, C. George, D.J. Beesley, J.J. Baumberg, M. De Volder, Photo-rechargeable organo-halide perovskite batteries, Nano Lett. 18 (2018) 1856–1862, https://doi.org/10.1021/acs.nanolett.7b05153.
[2] O. Nguyen, E. Courtin, F. Sauvage, N. Krins, C. Sanchez, C. Laberty-Robert, Shedding light on the light-driven lithium-ion de-insertion reaction: towards the design of a photo-rechargeable battery, J. Mater. Chem. A. 5 (2017) 5927–5933, https://doi.org/10.1039/C7TA00493A.
[3] C. Rodríguez-Seco, Y.-S. Wang, K. Zaghib, D. Ma, Photoactive nanomaterials enabled integrated photo-rechargeable batteries, Nanophotonics 11 (2022) 1443–1484, https://doi.org/10.1515/nanoph-2021-0782.
[4] B. Deka Boruah, A. Mathieson, S.K. Park, X. Zhang, B. Wen, L. Tan, A. Boies, M. De Volder, Vanadium dioxide cathodes for high-rate photo-rechargeable zinc-ion batteries, Adv. Energy Mater. 11 (2021) 2100115, https://doi.org/10.1002/aenm.202100115.
[5] B.D. Boruah, B. Wen, M. De Volder, Molybdenum disulfide-zinc oxide photocathodes for photo-rechargeable zinc-ion batteries, ACS Nano 15 (2021) 16616–16624, https://doi.org/10.1021/acsnano.1c06372.
[6] B.D. Boruah, A. Mathieson, B. Wen, S. Feldmann, W.M. Dose, M. De Volder, Photo-rechargeable zinc-ion batteries, Energy Environ. Sci. 13 (2020) 2414–2421, https://doi.org/10.1039/D0EE01392G.
[7] B. Deka Boruah, M. De Volder, Vanadium dioxide-zinc oxide stacked photocathodes for photo-rechargeable zinc-ion batteries, J. Mater. Chem. A. 9 (2021) 23199–23205, https://doi.org/10.1039/D1TA07572A.
[8] J. Zhao, Z. Xu, Z. Zhou, S. Xi, Y. Xia, Q. Zhang, L. Huang, L. Mei, Y. Jiang, J. Gao, Z. Zeng, C. Tan, A safe flexible self-powered wristband system by integrating defective MnO_{2-x} nanosheet-based zinc-ion batteries with perovskite solar cells, ACS Nano. 15 (2021) 10597–10608, https://doi.org/10.1021/acsnano.1c03341.
[9] B.D. Boruah, A. Mathieson, B. Wen, C. Jo, F. Deschler, M. De Volder, Photo-rechargeable zinc-ion capacitor using 2D graphitic carbon nitride, Nano Lett. 20 (2020) 5967–5974, https://doi.org/10.1021/acs.nanolett.0c01958.
[10] J. Bi, J. Zhang, P. Giannakou, T. Wickramanayake, X. Yao, M. Wang, X. Liu, M. Shkunov, W. Zhang, Y. Zhao, A highly integrated flexible photo-rechargeable system based on stable ultrahigh-rate quasi-solid-state zinc-ion micro-batteries and perovskite solar cells, Energy Stor. Mater. 51 (2022) 239–248, https://doi.org/10.1016/j.ensm.2022.06.043.
[11] H. Li, C. Xu, C. Han, Y. Chen, C. Wei, B. Li, F. Kang, Enhancement on cycle performance of Zn anodes by activated carbon modification for neutral rechargeable zinc ion batteries, J. Electrochem. Soc. 162 (8) (2015) A1439–A1444.
[12] N. Ma, P. Wu, Y. Wu, D. Jiang, G. Lei, Progress and perspective of aqueous zinc-ion battery, Funct. Mater. Lett. 12 (2019) 1930003, https://doi.org/10.1142/S1793604719300032.
[13] A.D. Salunke, S. Chamola, A. Mathieson, B.D. Boruah, M. de Volder, S. Ahmad, Photo-rechargeable Li-Ion batteries: device configurations, mechanisms, and materials, ACS Appl. Energy Mater. 5 (2022) 7891–7912, https://doi.org/10.1021/acsaem.2c01109.
[14] O. Ola, N. Wang, G. Walker, Y. Zhu, D. Grant, Engineering the next generation of photorechargeable Zinc-air batteries, Curr. Opin. Electrochem. 35 (2022), 101040, https://doi.org/10.1016/j.coelec.2022.101040.
[15] A. Paolella, C. Faure, G. Bertoni, S. Marras, A. Guerfi, A. Darwiche, P. Hovington, B. Commarieu, Z. Wang, M. Prato, M. Colombo, S. Monaco, W. Zhu, Z. Feng, A. Vijh, C. George, G.P. Demopoulos, M. Armand, K. Zaghib, Light-assisted delithiation of lithium iron phosphate nanocrystals towards photo-rechargeable lithium-ion batteries, Nat Commun. 8 (2017) 14643, https://doi.org/10.1038/ncomms14643.
[16] Y. Wang, J. Hu, L. Yu, X. Wu, Y. Zhang, H. Xu, Recent strategies for constructing efficient interfacial solar evaporation systems, Nano Res. (2023), https://doi.org/10.26599/NRE.2023.9120062.
[17] L. Ye, X. Peng, Z. Wen, H. Huang, Solid-State Z-scheme assisted hydrated tungsten trioxide/$ZnIn_2S_4$ photocatalyst for efficient photocatalytic H_2 production, Mater. Futures. 1 (3) (2022) 035103, https://doi.org/10.1088/2752-5724/ac7faf.
[18] C. Yang, R. Li, K.A.I. Zhang, W. Lin, K. Landfester, X. Wang, Heterogeneous photoredox flow chemistry for the scalable organo-synthesis of fine chemicals, Nat Commun. 11 (2020) 1239, https://doi.org/10.1038/s41467-020-14983-w.
[19] X. Li, X. Ma, Y. Hou, Z. Zhang, Y. Lu, Z. Huang, G. Liang, M. Li, Q. Yang, J. Ma, N. Li, B. Dong, Q. Huang, F. Chen, J. Fan, C. Zhi, Intrinsic voltage plateau of a Nb_2CT_x MXene cathode in an aqueous electrolyte induced by high-voltage scanning, Joule 5 (2021) 2993–3005, https://doi.org/10.1016/j.joule.2021.09.006.
[20] Y. Niu, S. Gong, X. Liu, C. Xu, M. Xu, S.-G. Sun, Z. Chen, Engineering iron-group bimetallic nanotubes as efficient bifunctional oxygen electrocatalysts for flexible Zn–air batteries, EScience 2 (2022) 546–556, https://doi.org/10.1016/j.esci.2022.05.001.
[21] G. Liang, X. Li, Y. Wang, S. Yang, Z. Huang, Q. Yang, D. Wang, B. Dong, M. Zhu, C. Zhi, Building durable aqueous K-ion capacitors based on MXene family, Nano Res. 1 (2022) e9120002, https://doi.org/10.26599/NRE.2022.9120002.
[22] A. Chithambararaj, A.C. Bose, Hydrothermal synthesis of hexagonal and orthorhombic MoO_3 nanoparticles, J. Alloys Compd. 509 (2011) 8105–8110, https://doi.org/10.1016/j.jallcom.2011.05.067.
[23] J. Gu, M.J. Hu, Q.Q. Guo, Z.F. Ding, X.L. Sun, J. Yang, High-yield synthesis of graphene quantum dots with strong green photoluminescence, RSC Adv. 4 (2014) 50141–50144, https://doi.org/10.1039/C4RA10011E.
[24] V. Kumar, X. Wang, P.S. Lee, Formation of hexagonal-molybdenum trioxide (h-MoO_3) nanostructures and their pseudocapacitive behavior, Nanoscale 7 (2015) 11777–11786, https://doi.org/10.1039/C5NR01505G.
[25] L. Zheng, Y. Xu, D. Jin, Y. Xie, Well-aligned molybdenum oxide nanorods on metal substrates: solution-based synthesis and their electrochemical capacitor application, J. Mater. Chem. 20 (2010) 7135, https://doi.org/10.1039/c0jm00744g.
[26] X.-F. Wang, G.-G. Wang, J.-B. Li, Z. Liu, Y.-X. Chen, L.-F. Liu, J.-C. Han, Direct white emissive Cl-doped graphene quantum dots-based flexible film as a single luminophore for remote tunable UV-WLEDs, Chem. Eng. J. 361 (2019) 773–782, https://doi.org/10.1016/j.cej.2018.12.131.

[27] X. Li, S.P. Lau, L. Tang, R. Ji, P. Yang, Multicolour light emission from chlorine-doped graphene quantum dots, J. Mater. Chem. C. 1 (2013) 7308, https://doi.org/10.1039/c3tc31473a.
[28] D. Sengupta, B. Mondal, K. Mukherjee, Visible light absorption and photo-sensitizing properties of spinach leaves and beetroot extracted natural dyes, Spectrochim. Acta, Part A 148 (2015) 85–92, https://doi.org/10.1016/j.saa.2015.03.120.
[29] L. Wang, Y. Li, Y. Wang, W. Kong, Q. Lu, X. Liu, D. Zhang, L. Qu, Chlorine-doped graphene quantum dots with enhanced anti- and pro-oxidant properties, ACS Appl. Mater. Interfaces 11 (2019) 21822–21829, https://doi.org/10.1021/acsami.9b03194.
[30] S.K. Cushing, M. Li, F. Huang, N. Wu, Origin of strong excitation wavelength dependent fluorescence of graphene oxide, ACS Nano 8 (2014) 1002–1013, https://doi.org/10.1021/nn405843d.
[31] P. Wongkrua, T. Thongtem, S. Thongtem, Synthesis of h- and α -MoO_3 by refluxing and calcination combination: phase and morphology transformation, photocatalysis, and photosensitization, J. Nanomater. 2013 (2013) 1–8, https://doi.org/10.1155/2013/702679.
[32] H. Hu, C. Deng, J. Xu, K. Zhang, M. Sun, Metastable h -MoO_3 and stable α -MoO_3 microstructures: controllable synthesis, growth mechanism and their enhanced photocatalytic activity, J. Exp. Nanosci. 10 (2015) 1336–1346, https://doi.org/10.1080/17458080.2015.1012654.
[33] W. Yu, W. Shang, Y. He, Z. Zhao, Y. Ma, P. Tan, Unraveling the mechanism of non-uniform zinc deposition in rechargeable zinc-based batteries with vertical orientation, Chem. Eng. J. 431 (2022), 134032, https://doi.org/10.1016/j.cej.2021.134032.
[34] W. Yuan, G. Ma, X. Nie, Y. Wang, S. Di, L. Wang, J. Wang, S. Shen, N. Zhang, In-situ construction of a hydroxide-based solid electrolyte interphase for robust zinc anodes, Chem. Eng. J. 431 (2022), 134076, https://doi.org/10.1016/j.cej.2021.134076.
[35] W. Zhuang, Q. Chen, Z. Hou, Z. Sun, T. Zhang, J. Wan, L. Huang, Examining concentration-reliant Zn deposition/stripping behavior in organic alcohol/sulfones-modified aqueous electrolytes, Small. 2300274. https://doi.org/10.1002/smll.202300274.